

Grand-potential phase field simulations of droplet growth and sedimentation in a two-phase ternary fluid

Werner Verdier^{1,2}, Alain Cartalade¹, Mathis Plapp^{2*}

¹ Université Paris-Saclay, CEA, Service de Thermo-hydraulique et de Mécanique des Fluides, 91191 Gif-sur-Yvette, France

² Laboratoire de Physique de la Matière Condensée, CNRS, École Polytechnique, Institut Polytechnique de Paris, 91120 Palaiseau, France

Abstract

A methodology is built to model and simulate the dynamics of domain coarsening of a two-phase ternary liquid with an arbitrary phase diagram. High numerical performance is obtained through the use of the phase field-method for interface capturing, a lattice Boltzmann method numerical scheme for all the model equations, and a portable, parallel simulation code running on multiple GPUs. The model is benchmarked against an analytic solution for a ternary diffusion couple. It also reproduces the well-known power law for droplet coarsening during Ostwald ripening without fluid flow. Large-scale simulations with flow illustrate the effects of momentum transport and buoyancy, as well as droplet coalescence and sedimentation.

Keywords: Phase-field models, Phase separation, Multicomponent mixtures, Lattice-Boltzmann method

*Corresponding author, mathis.plapp@polytechnique.fr

1 Introduction

When a homogeneous solid or liquid mixture is rapidly quenched into a thermodynamically unstable state, phase separation occurs. After an initial stage of spinodal decomposition, during which microscopic fluctuations are amplified with time, spatial domains of the new equilibrium phases form and are separated by well-defined interfaces with a characteristic thickness. At later times, domain coarsening occurs: under the driving force of capillarity, the total interface area is progressively reduced by the elimination of geometric features with high curvature, such as protrusions or small domains.

This phenomenon has been extensively studied because it provides an example of a system that never reaches equilibrium, but instead exhibits scaling laws [1]. Indeed, in a system of infinite size, domain coarsening continues indefinitely and leads to patterns that are scale-invariant, that is, the structure and geometry of the pattern is statistically invariant in time, and only its overall scale grows with time as a power law. The growth exponent depends on the underlying transport processes (diffusion, hydrodynamics [2], or elasticity) and on the nature of the order parameter that describes the domain (scalar, vector or tensor, conserved or non-conserved) [3, 4].

Besides its theoretical interest, phase separation is also important for a large number of industrially relevant processes, such as the formation of porous glasses and membranes. One example that motivated the present work is the conditioning of nuclear waste in glass: the radioactive substances are mixed with a glass matrix, a mixture of glass formers that is optimized for long-term resistance to environmental stresses [5]. In order to increase the amount of waste, glass ceramics are being studied as an alternative to conventional glass. For a simplified ternary system, a liquid-liquid phase separation can occur when its global composition lies within a miscibility gap. The composition of the first liquid phase is representative of waste, whereas the composition of the second one is representative of the glass matrix [6, 7].

For the study of generic features of phase separation, such as spinodal decomposition dynamics and scaling laws in coarsening, the Cahn-Hilliard equation [8] and its various generalizations have been extensively used. Its appealing feature is that it can be simply derived from out-of-equilibrium thermodynamics, taking as a starting point the description of heterogeneous systems by a free-energy functional. The Cahn-Hilliard equation can describe the complete time evolution of a phase-separating system, from the initial

spinodal decomposition to the late-stage coarsening, if transport is governed by diffusion. It can be coupled with the Navier-Stokes equation [9, 10] to model coarsening that is mediated by hydrodynamics, as well as the crossover between different coarsening regimes [11, 12].

While the Cahn-Hilliard equation is thus an excellent tool to explore generic features of phase-separating systems, it is rather difficult to adapt it for the description of specific materials. There are two reasons for this. Firstly, the Cahn-Hilliard equation is formulated for a binary system, with a concentration as the only dynamic variable, and a free-energy functional that consists of a double-well potential and a gradient term. In this formulation, the interface free energy is controlled by the interplay of these two terms. It is therefore difficult to modify the bulk thermodynamic properties, which are set by the curvature of the free-energy function, while leaving the interface energy invariant [13]. Secondly, for multi-component mixtures, there are several independent chemical compositions, and the gradient energy coefficient becomes a symmetric matrix, with entries that are in principle determined by the pairwise interaction between the different components. However, since those are not directly known, the system is underdetermined, that is, for a target interface energy, there are many possible choices for the gradient coefficients. This choice has non-trivial consequences for the interface structure: interface adsorption of certain components can occur, which modifies the interface energy and the macroscopic conservation laws for moving interfaces [14].

An alternative way for describing interfaces in multicomponent mixtures has been developed in the framework of phase-field theory [15, 16, 17]. The interface is described by a scalar phase field, which can be seen as a smoothed indicator function (with 1 and 0 corresponding to presence or absence of the phase). The equation of motion for this field derives from a Ginzburg-Landau free energy functional and is coupled to the concentration fields. The latter are then governed by their own free energy functions, which do not come into play for the determination of the interface properties, and which can therefore be chosen at will. The connection between the phase-field model and the more traditional free-boundary problem can be made using the well-established technique of matched asymptotic expansions [18, 19, 20, 21].

For the quantitative description of moving interfaces in multi-component mixtures, the grand-potential model (which is a reformulation of the earlier Kim-Kim-Suzuki model [22]) has been widely used and benchmarked [23, 24, 25]. It corresponds to a grand-canonical formulation of the mixture

thermodynamics, with the chemical potentials as basic variables, which is suitable because two phases that coexist in a mixture have different compositions but equal chemical potentials.

Here, we couple a grand-canonical phase-field model for multicomponent mixtures with a description of fluid flow using the lattice-Boltzmann method (LBM) [26] to achieve a model for domain coarsening that can be used for specific substances with given thermodynamics (obtained, for example, from a CALPHAD database [27]). This model cannot describe the initial stages of spinodal decomposition, because the grand-potential formulation requires a monotonic relation between composition and chemical potentials, but it provides a quantitative description of the late-stage domain coarsening regime. Since, in real substances, the two phases generally do not have the same density, we include buoyancy in the model, which makes it possible to describe sedimentation of droplets of the heavier phase.

We develop an implementation in which all the equations, including the phase-field model, are solved within the LBM formalism [26]. Indeed, while LBM was initially developed for fluid flow, it was soon recognized that it is a general method for the time integration of partial differential equations, and we have previously used this formulation for solidification problems [28]. The advantage is that the simulation code is entirely formulated in the LBM framework, and therefore high-performance algorithms developed for LBM can be used. In particular, LBM is well adapted for GPU parallelization.

In the present manuscript, we will first describe the grand-potential phase-field model we use, which is similar to previously published work. Specifically, we model a two-phase three-component fluid. We will then detail our numerical implementation, and present a detailed benchmark study on a ternary diffusion couple, which shows that non-trivial interface conditions can be accurately resolved by our formulation. Then, we present simulations of domain coarsening, in two dimension without fluid flow as a benchmark, and in three dimensions with fluid flow, in a large system which contains many droplets. These simulations are carried out with the high-performance computing code LBM_Saclay [29]. These illustrative simulations demonstrate that our code can be used to perform large-scale studies, and thus is a suitable tool for the investigation of practical problems.

2 Model

2.1 Thermodynamics

We consider a ternary mixture, and denote by $c^A(\mathbf{x}, t)$, $c^B(\mathbf{x}, t)$, and $c^C(\mathbf{x}, t)$ the local molar fractions of the A , B , and C components. Since $c^A + c^B + c^C = 1$, only two concentration fields are independent; we choose to eliminate c^C by writing $c^C = 1 - c^A - c^B$, and write the (Helmholtz) free energy density of a homogeneous system as $f(c^A, c^B)$. For a specific substance, this free energy function can be typically obtained from a CALPHAD [27] database. Such a database usually gives the molar Gibbs free energy, but we will suppose that the molar volume is constant and independent of the composition, so that Gibbs and Helmholtz free energies are equivalent. The variables that are thermodynamically conjugate to the compositions are the diffusion potentials, that is, the difference of the chemical potentials of A and C and B and C , respectively,

$$\mu^\alpha = V_a \frac{\partial f}{\partial c^\alpha} \quad (\alpha = A, B) \quad (1)$$

where V_a is the atomic volume (the molar volume divided by Avogadro's number). This factor has been included to give the diffusion potentials (which will also be called chemical potentials in the following) their usual dimension of energy [25].

For a phase-separating system, the “free energy landscape” $f(c^A, c^B)$ has a double-well structure, with two convex regions separated by a concave one; the latter corresponds to the compositions for which a homogeneous system is thermodynamically unstable. At equilibrium, the system is in a coexistence of two phases, called “phase 0” and “phase 1” in the following, which have different compositions, each one being located in one of the wells of the free energy function. Minimization of the free energy under the constraint of global mass conservation yields the conditions for phase coexistence:

$$V_a \left. \frac{\partial f_0}{\partial c^\alpha} \right|_{c_0^{\alpha, \text{eq}}} = V_a \left. \frac{\partial f_1}{\partial c^\alpha} \right|_{c_1^{\alpha, \text{eq}}} = \mu^{\alpha, \text{eq}}, \quad (2)$$

$$\begin{aligned} f_0(c_0^{A, \text{eq}}, c_0^{B, \text{eq}}) - f_1(c_1^{A, \text{eq}}, c_1^{B, \text{eq}}) \\ = \frac{1}{V_a} \sum_{\alpha=A, B} \mu^{\alpha, \text{eq}} (c_0^{\alpha, \text{eq}} - c_1^{\alpha, \text{eq}}), \end{aligned} \quad (3)$$

where $\mu^{\alpha,\text{eq}}$, $c_0^{\alpha,\text{eq}}$, and $c_1^{\alpha,\text{eq}}$ are the chemical potentials and the compositions of phase 0 and 1 at two-phase equilibrium. Geometrically, this corresponds to a “common tangent plane” to the free energy landscape. From this geometric picture, or from a simple counting of degrees of freedom (three equations for four unknown equilibrium compositions), it is clear that the solution to these equations is not unique. In the space of compositions, which is usually visualized in the Gibbs simplex, the various possible equilibria are indicated by *tie lines* (see Figure 1 below). The global equilibrium corresponds to the unique tie line which contains the composition inventory (the average composition) of the closed system.

The conditions for phase coexistence can be conveniently reformulated in the grand-canonical framework for open system, in which the fundamental variables are the diffusion potentials, and the relevant thermodynamic potential is the grand potential,

$$\omega(\mu^A, \mu^B) = f(c^A(\mu^A, \mu^B), c^B(\mu^A, \mu^B)) - \frac{1}{V_a} \sum_{\alpha=A,B} \mu^\alpha c^\alpha(\mu^A, \mu^B), \quad (4)$$

which is the Legendre transform of the free energy. In writing down this formula, we have supposed that the functions $\mu^\alpha(c^A, c^B)$ can be inverted to yield $c^\alpha(\mu^A, \mu^B)$. This is guaranteed only if these functions are monotonous, which corresponds to a convex free energy landscape. In the case of a phase-separating system, the Legendre transform must be taken separately for each convex region in composition space (see below for details), which yields two different grand potential functions for the two phases, ω_0 and ω_1 . Phase coexistence is then simply given by

$$\omega_0(\mu^A, \mu^B) = \omega_1(\mu^A, \mu^B). \quad (5)$$

This defines a coexistence line in the space of the intensive variables (the two diffusion potentials), each point of which corresponds to a tie line in composition space.

In general, the calculation of the Legendre transform in Eq. (4) cannot be performed analytically, since free energy functions typically involve both polynomials and logarithms of the concentrations. It can always be performed numerically, but in the case of interest here we can exploit the fact that during the late stages of the phase separation process, the concentrations will be close to the global equilibrium concentrations. Therefore, only the vicinity in concentration space of the reference equilibrium is relevant, and we

can perform a second-order Taylor expansion of the free energy around the equilibrium concentrations for each phase, as was already done in previous works [24],

$$\begin{aligned}
f_\pi(c^A, c^B) &= f_\pi(c_\pi^{A,\text{eq}}, c_\pi^{B,\text{eq}}) + \sum_\alpha \frac{\mu^{\alpha,\text{eq}}}{V_a} (c^\alpha - c_\pi^{\alpha,\text{eq}}) \\
&\quad + \frac{1}{2} \sum_{\alpha,\beta} K_\pi^{\alpha\beta} (c^\alpha - c_\pi^{\alpha,\text{eq}})(c^\beta - c_\pi^{\beta,\text{eq}}). \tag{6}
\end{aligned}$$

Here and in the remainder of the text, exponents in Greek letters and the index π identify components A or B , and phase 0 or 1, respectively. In Eq. (6), we have used Eq. (1) in the first order terms, and the second order coefficients are given by

$$K_\pi^{\alpha\beta} = \left. \frac{\partial^2 f}{\partial c^\alpha \partial c^\beta} \right|_{c_\pi^{A,\text{eq}}, c_\pi^{B,\text{eq}}}. \tag{7}$$

In this quadratic approximation, Eq. (1) yields a linear relation between the chemical potentials and the compositions,

$$\mu_\pi^\alpha(c^A, c^B) = \mu^{\alpha,\text{eq}} + K_\pi^{\alpha A} (c^A - c_\pi^{A,\text{eq}}) + K_\pi^{\alpha B} (c^B - c_\pi^{B,\text{eq}}). \tag{8}$$

This equation can easily be inverted to obtain $c^\alpha(\mu^A, \mu^B)$, which, together with Eq. (4), yields an analytic approximation for the grand potential.

The procedure outlined above is valid in the late stage of phase separation for arbitrary free energy functions. Since, in the present contribution, we do not intend to model a particular material, but are rather interested in benchmark calculations, we choose as an example a simple model system, in which the matrix of second order coefficients is diagonal, with equal values for the two phases,

$$K_\pi^{\alpha\beta} = K \delta_{\alpha\beta}, \tag{9}$$

where $\delta_{\alpha\beta}$ is the Kronecker symbol. This corresponds to circular parabolic free energy wells with equal curvatures for both phases. Furthermore, we will switch to the new variables $\tilde{\mu}^\alpha = \mu^\alpha - \mu^{\alpha,\text{eq}}$ and $\tilde{\omega}_\pi = \omega_\pi(\mu^A, \mu^B) - \omega_\pi(\mu^{A,\text{eq}}, \mu^{B,\text{eq}})$, which amounts to choosing the reference values for the chemical potentials and the grand potential. In these variables, the grand potentials can be expressed as

$$\tilde{\omega}_\pi(\tilde{\mu}^A, \tilde{\mu}^B) = -\frac{1}{2KV_a^2} \sum_{\alpha=A,B} (\tilde{\mu}^\alpha)^2 - \frac{1}{V_a} \sum_{\alpha=A,B} \tilde{\mu}^\alpha c_\pi^{\alpha,\text{eq}}. \tag{10}$$

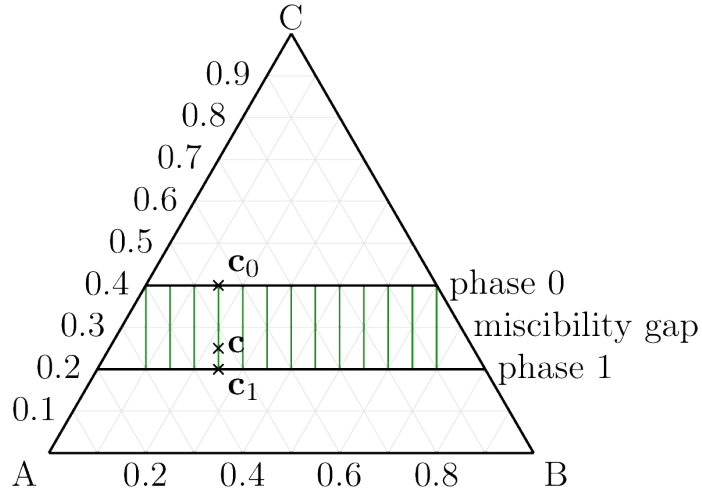


Figure 1: Ternary phase diagram of the idealized material considered in this work. It arises from the quadratic free energies with identical second derivatives for each phases. The horizontal black lines are the phase boundaries and the green lines are some of the tie-lines. Each of these tie-lines defines a valid chemical equilibrium with the compositions of each phase located at each end of the line.

The phase diagram obtained from this model with $c_0^{A,\text{eq}} = c_0^{B,\text{eq}} = 0.3$ and $c_1^{A,\text{eq}} = c_1^{B,\text{eq}} = 0.4$ is displayed in Figure 1.

2.2 Grand potential phase field formalism

In a multi-component Cahn-Hilliard model, the free energy landscape defined above would be supplemented by square gradient terms in the free energy functional to capture the free energy cost of inhomogeneities, which then adds non-local terms (containing Laplace operators) to the diffusion potentials. Instead, we choose to describe phases and interfaces by an additional scalar phase field $\varphi(\mathbf{x}, t)$, with values in $[0, 1]$, whose extrema identify one of the two bulk liquid phase. The smooth variations of φ will locate the diffuse interfaces.

The model is based on a phenomenological grand potential functional [23, 24, 25] over the volume V of the system, function of the phase field φ

and of the fields of intensive thermodynamical variables μ^A, μ^B ,

$$\Omega[\varphi, \mu^A, \mu^B] = \int_V (\omega_{\text{int}}(\varphi) + \omega_{\text{th}}(\varphi, \mu^A, \mu^B)). \quad (11)$$

The two contributions describe the interfacial and bulk (thermodynamic) contributions to the total grand potential, respectively.

The interfacial part,

$$\omega_{\text{int}}(\varphi) = \frac{\zeta}{2} |\nabla\varphi|^2 + H\omega_{\text{dw}}(\varphi), \quad (12)$$

contains a square gradient energy term and the double-well function $\omega_{\text{dw}}(\varphi) = 8\varphi^2(1 - \varphi)^2$. They are parametrized by the characteristic energy scales H ($[E] \cdot L^{-3}$, height of the double-well) and ζ ($[E] \cdot L^{-1}$, gradient energy coefficient). The system evolves to minimize Ω : the double-well term, favoring a sharp profile for φ at the interface, will then play against the gradient energy term, which favors smooth variations of φ . Assuming a plane interface at equilibrium (where the bulk term ω_{th} is absent), the interface solution is given by the hyperbolic tangent profile

$$\varphi_0(x) = \frac{1}{2} (1 + \tanh(2x/W)), \quad (13)$$

with

$$W = \sqrt{\zeta/H} \quad (14)$$

the characteristic interface width. Reintroducing this profile in the integral (11) gives a characteristic value of the surface tension due to the diffuse interface,

$$\sigma = \frac{2}{3}HW. \quad (15)$$

This relation also identifies H as the characteristic energy-per-volume scale of the excess free energy stored in the diffuse interface. More details about these calculations can be found in introductory texts about the phase-field method, for example in Refs. [30, 15, 25].

The bulk contribution is an interpolation between the grand potentials of the two phases,

$$\omega(\varphi, \mu^A, \mu^B) = [1 - p(\varphi)]\omega_0(\mu^A, \mu^B) + p(\varphi)\omega_1(\mu^A, \mu^B), \quad (16)$$

with $p(\varphi) = 3\varphi^2 - 2\varphi^3$ an interpolation function odd around $\varphi = 1/2$, satisfying $p(\{0, 1\}) = \{0, 1\}$ and $p'(\{0, 1\}) = 0$, that can be seen as a smoothed step function [25].

The interface-tracking equation, also known as the Allen-Cahn equation, is obtained by relating linearly the time evolution of φ and the decrease in Ω , expressed as the variational derivative,

$$\partial_t \varphi = -M_\varphi \frac{\delta \Omega}{\delta \varphi}. \quad (17)$$

Here, M_φ is a kinetic coefficient (phase-field mobility). The terms in this equations that are generated from the interfacial energy stabilize the interface profile, whereas the bulk term creates a driving force for interface motion if the grand potentials of the two phases differ.

It is convenient to remove the energy dimensions: define the dimensionless chemical potentials $\bar{\mu}^\alpha = \tilde{\mu}^\alpha / (KV_a)$, and

$$\begin{aligned} \bar{\omega}_\pi(\bar{\mu}^A, \bar{\mu}^B) &= \tilde{\omega}_\pi(\tilde{\mu}^A, \tilde{\mu}^B) / K \\ &= -\frac{1}{2} \sum_{\alpha=A,B} ((\bar{\mu}^\alpha)^2 + 2\bar{\mu}^\alpha c_\pi^{\alpha,\text{eq}}). \end{aligned} \quad (18)$$

We can now write the interface tracking equation (17) in terms of the fields φ , $\bar{\mu}^A$ and $\bar{\mu}^B$ as

$$\tau_\varphi \partial_t \varphi = W^2 \nabla^2 \varphi - \omega'_{\text{dw}}(\varphi) + \lambda p'(\varphi) \Delta \bar{\omega}(\bar{\mu}^A, \bar{\mu}^B) \quad (19)$$

with the phase-field relaxation time $\tau_\varphi = 1/(M_\varphi H)$ and the difference of the grand potential densities

$$\begin{aligned} \Delta \bar{\omega} &= \bar{\omega}_0 - \bar{\omega}_1 \\ &= - \sum_{\alpha=A,B} \bar{\mu}^\alpha (c_0^{\alpha,\text{eq}} - c_1^{\alpha,\text{eq}}), \end{aligned} \quad (20)$$

where the thermodynamical coupling parameter is $\lambda = K/H$. We also define the scaled phase-field mobility $\bar{M}_\varphi = M_\varphi H = W^2/\tau_\varphi$, which has the dimension of a diffusion coefficient.

2.3 Species diffusion and mixed formulation

In the absence of hydrodynamic flow, the redistribution of chemical species occurs by diffusion. The concentration of each species is a locally conserved

quantity, hence

$$\partial_t c^\alpha(\mathbf{x}, t) = -\nabla \cdot \mathbf{j}^\alpha(\mathbf{x}, t). \quad (21)$$

According to the thermodynamics of irreversible processes, the species currents write

$$\mathbf{j}^\alpha(\mathbf{x}, t) = - \sum_{\beta=A,B} M^{\alpha\beta} \nabla \mu^\beta, \quad (22)$$

where $M^{\alpha\beta}$ are the components of the atomic mobility matrix. Furthermore, in the grand-canonical setting, where the natural variables are the chemical potentials, the composition can be obtained from the grand-potential functional by

$$c^\alpha = -V_a \frac{\delta \Omega}{\delta \mu^\alpha} = -V_a \left(p(1 - \varphi) \frac{\partial \bar{\omega}_0}{\partial \bar{\mu}^\alpha} + p(\varphi) \frac{\partial \bar{\omega}_1}{\partial \bar{\mu}^\alpha} \right). \quad (23)$$

In the original grand-potential method for a binary alloy [23], the concentration was eliminated from Eq. (21) in favor of the chemical potential; however, for multi-component alloys, this requires numerous matrix inversions [24]. Therefore, we prefer to use a mixed formulation, as in some previous works [31, 32]: we keep both the concentrations and the compositions as dynamic variables. This allows to solve Eq. (21), using the explicit algorithm of one's choice to update c^α ; μ^α is then updated by inverting Eq. (23). Remark that the inversion step has a simple analytical expression with the quadratic free energies, namely

$$\bar{\mu}^\alpha = c^\alpha - p(1 - \varphi) c_0^{\alpha, \text{eq}} - p(\varphi) c_1^{\alpha, \text{eq}}. \quad (24)$$

Here, we will use a diagonal mobility matrix and remove the dimension of energy by defining $\bar{M}^\alpha = K M^{\alpha\alpha}$; \bar{M}^α then has the dimension of a diffusion coefficient. If the diffusion coefficient is different in the two phases, the mobility is linearly interpolated, $\bar{M}^\alpha(\varphi) = \bar{M}_0^\alpha(1 - \varphi) + \bar{M}_1^\alpha\varphi$ for both components $\alpha = A, B$. Notice that in the bulk phases, Eq. (21) reduces to Fick's laws with fluxes $\bar{M}^\alpha \nabla c^\alpha$ because of the quadratic free energies. This will be helpful in preliminary tests since analytical solutions are available in this case (*cf.* sec. 4.1).

2.4 Equivalent sharp-interface model

The fact that phase field models only track an implicit, diffuse interface greatly facilitates the numerical treatment of two-phase problems. However,

the behavior of the physical variables other than φ at the phase interface is at first glance unspecified. This is in contrast to the sharp-interface formulations of free-boundary problems, whose well-posedness depends on the presence of explicit boundary condition at the interface for values and fluxes of the relevant transport fields.

An important effort in the phase field literature is made to bridge both formulations by extracting implicit interface conditions from the phase field equations in the asymptotic limit of small W (“thin-interface limit”), and to add corrections if necessary to obtain adjustable interface properties. This is done using the formalism of matched asymptotic analysis in terms of an asymptotic parameter ε expressing the scale separation between the interface thickness and the physically relevant “outer” scales. As this process is lengthy and has already been presented in much detail in other works, we will only present its results here. The interested reader can refer to [19] for a step-by-step detail of the calculations ; to [33] and [21] for a more detailed definition of the curvilinear coordinates and subsequent reexpression of the differential operators ; and to [18] and then [20] for a discussion of what can be considered a “thin” interface.

The asymptotic analysis of the model without flow was realized following the formalism of Almgren [19]. It was seen that the case of a ternary system or the presence of a closure relation, Eq. (23), introduce little novelty in the calculations. The result is a Gibbs-Thomson relation for the grand potential at the interface,

$$\Delta\bar{\omega} = -\delta\kappa - \beta V \quad (25)$$

with κ the local curvature of the interface, V its normal velocity, and the associated coefficients are

$$\delta = \frac{2}{3} \frac{W}{\lambda} \quad (26)$$

$$\beta = \frac{2}{3} \frac{W}{\lambda M_\varphi} - \frac{19}{120} \sum_{\alpha=A,B} \frac{W(c_0^{\alpha,\text{eq}} - c_1^{\alpha,\text{eq}})^2}{\bar{M}^\alpha} \quad (27)$$

The numerical factors are due to integrations across the diffuse interface profile and depend on the choice of the double-well function and the interpolation function $p(\varphi)$. The asymptotics also yields the composition balance at the interface,

$$V[c^\alpha]_-^+ = - [\bar{M}^\alpha \partial_n \bar{\mu}^\alpha]_-^+ \quad (28)$$

where $[\cdot]^\pm$ denotes the jump of a field across the interface, and ∂_n the gradient projected on the interface normal.

2.5 Flow coupling

To include hydrodynamic flow dynamics, we couple our phase-field model to the incompressible Navier-Stokes equation,

$$\nabla \cdot \mathbf{u} = 0 \quad (29)$$

$$\rho_0 [\partial_t \mathbf{u} + \nabla \cdot (\mathbf{u}\mathbf{u})] = -\nabla p_h + \nabla \cdot [\rho_0 \nu(\varphi)(\nabla \mathbf{u} + \nabla \mathbf{u}^T)] + \mathbf{F}_{tot} \quad (30)$$

$$\partial_t \varphi + \mathbf{u} \cdot \nabla \varphi = \frac{W^2}{\tau_\varphi} \nabla^2 \varphi - \frac{1}{\tau_\varphi} \omega'_{dw}(\varphi) + \frac{\lambda}{\tau_\varphi} p'(\varphi) \Delta \bar{\omega}(\bar{\mu}^A, \bar{\mu}^B) \quad (31)$$

$$\partial_t c^\alpha + \mathbf{u} \cdot \nabla c^\alpha = \nabla \cdot [\bar{M}^\alpha(\varphi) \nabla \bar{\mu}^\alpha] \quad (32)$$

$$\bar{\mu}^\alpha = c^\alpha - p(1 - \varphi) c_0^{\alpha, \text{eq}} - p(\varphi) c_1^{\alpha, \text{eq}} \quad (33)$$

where \mathbf{u} is a phase-averaged velocity field [34, 21], ρ_0 is the constant density, p_h is the hydrodynamic pressure enforcing the condition $\nabla \cdot \mathbf{u} = 0$ (Lagrange multiplier of that condition), $\nu(\varphi)$ is the (phase-dependent) kinematic viscosity, the component index α is A, B and the total force \mathbf{F}_{tot} is the sum of the gravity force $\mathbf{F}_g = \varphi \Delta \rho \mathbf{g}$ in the Boussinesq approximation (with $\Delta \rho$ the density different between the phases, phase 1 being denser than phase 0, and \mathbf{g} the constant acceleration vector due to gravity) and the surface tension force \mathbf{F}_σ defined by [9, 10]:

$$\mathbf{F}_\sigma = \frac{3}{2} \sigma W \left[\frac{\omega'_{dw}(\varphi)}{W^2} - \nabla^2 \varphi \right] \nabla \varphi \quad (34)$$

For the equilibrium solution $\varphi = \varphi_0$, the term inside the bracket is equivalent to $\kappa |\nabla \varphi|$ where κ is the curvature defined by $\kappa = -\nabla \cdot \mathbf{n}$. The surface tension force can be expressed by $\mathbf{F}_s = \delta_d \sigma \kappa \mathbf{n}$, i.e. the quantity $\sigma \kappa \mathbf{n}$ is spread over $\delta_d = (3/2)W |\nabla \varphi|^2$ where W is the thickness of the diffuse interface.

In the phase-field equation Eq. (31), for simplifying the notations in the next Section, we define the following source term:

$$\mathcal{S}_\varphi(\varphi, \bar{\mu}^A, \bar{\mu}^B) = -\frac{1}{\tau_\varphi} \omega'_{dw}(\varphi) + \frac{\lambda}{\tau_\varphi} p'(\varphi) \Delta \bar{\omega}(\bar{\mu}^A, \bar{\mu}^B) \quad (35)$$

which contains the contributions of the double-well (first term) and the thermodynamic imbalance $\Delta \bar{\omega}$ (second term) responsible for the displacement of

the interface. For $\mathbf{u} = \mathbf{0}$, the interface is displaced by diffusion until the thermodynamic equilibrium is reached, i.e. when the grand-potential densities of each phase are equal $\bar{\omega}_0(\bar{\mu}^A, \bar{\mu}^B) = \bar{\omega}_1(\bar{\mu}^A, \bar{\mu}^B)$.

3 Lattice Boltzmann Method

The numerical resolution of the model is done through the LBM, which consists of a discretization of the Boltzmann equation in phase-space. This defines a regular lattice, and the time-explicit resolution of the equation is assimilable to the distribution functions undergoing a collision step on the nodes followed by a transport step along the edges. According to the choice of collision operator (here the simple BGK operator), of equilibrium functions, and of additional source and force terms, the moments of the distribution function thus solved can be shown to be solution of conservative time-evolution PDEs such as the ones of the present model. This is coherent with a discretized Chapman-Enskog expansion.

LBM is a very popular method to simulate various conservative PDEs and more particularly the Navier-Stokes equations. For those latter ones, more traditional methods use a prediction-correction algorithm that requires solving a time-consuming Poisson equation. The LBM benefits from the efficiency of the equivalent artificial compressibility algorithm. The collision operator is local and each discrete distribution function follows an identical evolution equation. The method is therefore very simple to implement and is parallel in nature by efficiently exploiting the shared memory. Moreover, coupled with a distributed memory parallelism (e.g. MPI), that algorithm is very efficient. The interested reader can refer to references such as [26] for more details on the LBM.

In this work, the standard D2Q9 and D3Q19 lattices are used for all 2D or 3D simulations, respectively. Those lattices correspond to a discretization of the velocity-space with 9 or 19 discrete velocities \mathbf{c}_k defined by $\mathbf{c}_k = (\delta x / \delta t) \mathbf{e}_k$ with δx the space step, δt the time step, and \mathbf{e}_k the direction vectors. Each set of directions is weighted by a scalar value w_k . The directions \mathbf{e}_k and their weights are listed in Table 1a for D2Q9 and Table 1b for D3Q19.

We also define a characteristic speed c_s defined by $c_s = (1/\sqrt{3})\delta x/\delta t$. The distribution functions and the discrete Lattice Boltzmann equations (LBE) with the BGK collision operator are detailed next in Section 3.1 for fluid flow, in section 3.2 for phase-field and in Section 3.3 for the compo-

k	\mathbf{e}_k				w_k
0	(0, 0)				4/9
1, 2, 3, 4	(+1, 0)	(0, +1)	(-1, 0)	(0, -1)	1/9
5, 6, 7, 8	(+1, +1)	(-1, +1)	(-1, -1)	(+1, -1)	1/36

(a) Lattice D2Q9.

k	\mathbf{e}_k			w_k
0	(0, 0, 0)			1/3
1, 2, 3	(+1, 0, 0)	(-1, 0, 0)	(0, +1, 0)	1/18
4, 5, 6	(0, -1, 0)	(0, 0, +1)	(0, 0, -1)	
7, 8, 9	(+1, +1, 0)	(-1, -1, 0)	(+1, 0, +1)	1/36
10, 11, 12	(-1, 0, -1)	(0, +1, +1)	(0, -1, -1)	
13, 14, 15	(+1, -1, 0)	(-1, +1, 0)	(+1, 0, -1)	
16, 17, 18	(-1, 0, +1)	(0, +1, -1)	(0, -1, +1)	

(b) Lattice D3Q19

Table 1: Detail of the direction vectors \mathbf{e}_k and scalar weights w_k associated to each velocity of the D2Q9 (1a) and D3Q19 (1b) lattices.

sition equations. Many alternative collision operators exist in LBM literature. The most popular operators are the "Two-Relaxation-Times" (TRT) and "Multiple-Relaxation-Times" (MRT) which define respectively two (for TRT) or more (for MRT) additional collision rates to tune for improving stability and accuracy. Here, we present a proof of concept of a thermodynamic model that is based on the grand-potential functional and coupled with fluid flow. The ratio of diffusion coefficients are almost 1 and the kinematic viscosity of each phase is identical. The BGK operator is sufficient in this work.

3.1 LBM for fluid flow

For simulating the fluid flow, the numerical scheme works on the distribution function $f_k(\mathbf{x}, t)$ for which its evolution is given by the lattice Boltzmann

equation:

$$f_k(\mathbf{x} + \mathbf{c}_k \delta t, t + \delta t) = f_k(\mathbf{x}, t) - \frac{1}{\tau_f(\varphi) + 0.5} [f_k(\mathbf{x}, t) - f_k^{eq}(\mathbf{x}, t)] + \delta t \mathcal{F}_k(\mathbf{x}, t) \quad (36)$$

where the relaxation rate τ_f is related to the kinematic viscosity by $\nu(\varphi) = \tau_f(\varphi) c_s^2 \delta t$ and the source term $\mathcal{F}_k(\mathbf{x}, t)$ contains the total force term \mathbf{F}_{tot} of Eq. (30). Several forcing schemes exist in the LBM literature, here we choose one of the two most popular methods [35]:

$$\mathcal{F}_k(\mathbf{x}, t) = \Gamma_k(\mathbf{x}, t) (\mathbf{c}_k - \mathbf{u}) \cdot \mathbf{F}_{tot} \quad (37)$$

$$\Gamma_k(\mathbf{x}, t) = w_k \left[1 + \frac{\mathbf{c}_k \cdot \mathbf{u}}{c_s^2} + \frac{(\mathbf{c}_k \cdot \mathbf{u})^2}{2c_s^4} - \frac{\mathbf{u}^2}{2c_s^2} \right] \quad (38)$$

The moment of order zero of Eq. (37) is $\sum_k \mathcal{F}_k = 0$ and its moment of first-order is equal to $\sum_k \mathcal{F}_k \mathbf{c}_k = \mathbf{F}_{tot}$. For recovering the incompressible Navier-Stokes equation with the Chapman-Enskog expansion, the equilibrium distribution function f_k^{eq} has to be defined by [36]:

$$f_k^{eq}(\mathbf{x}, t) = w_k \left[p_h + \rho_0 c_s^2 \left(\frac{\mathbf{c}_k \cdot \mathbf{u}}{c_s^2} + \frac{(\mathbf{c}_k \cdot \mathbf{u})^2}{2c_s^4} - \frac{\mathbf{u}^2}{2c_s^2} \right) \right] - \frac{\delta t}{2} \mathcal{F}_k \quad (39)$$

where the term $\mathcal{F}_k \delta t / 2$ has been subtracted for capturing the second-order accuracy when the external force term is taking into account in Eq. (36). That trick is equivalent to a change of variables in the distribution function to conserve an explicit algorithm after the trapezoidal integration of the Boltzmann equation. Because of that change of variables, the term $\sum_k \mathcal{F}_k \mathbf{c}_k \delta t / 2$ must be added for updating the velocity for each time-step. After collision and streaming, the hydrodynamic pressure is obtained by the moment of order zero of f_k , and the velocity by the moment of first order:

$$p_h = \sum_k f_k \quad (40)$$

$$\rho_0 \mathbf{u} = \frac{1}{c_s^2} \sum_k f_k \mathbf{c}_k + \frac{\delta t}{2} \mathbf{F}_{tot} \quad (41)$$

When a high contrast of density exists between both phases, another popular method is widely applied for defining the equilibrium distribution function f_k^{eq} . In that case, the density becomes an interpolation of the bulk density of each phase (e.g. $\varrho(\varphi)$), and a dimensionless pressure $p^* = p_h/\varrho(\varphi)c_s^2$ is introduced in the equilibrium Eq. (39) [37]. In that case, two supplementary forces must be added in \mathbf{F}_{tot} , the pressure and viscosity forces [38], in order to recover the incompressible Navier-Stokes. Here, we assume that the density is identical in both phases, so that the classical equilibrium Eq. (39) is sufficient for the simulations.

The surface tension force Eq. (34) requires computing a gradient term and a laplacian term. The gradient is evaluated by the directional derivatives:

$$\mathbf{e}_k \cdot \nabla \varphi|_{\mathbf{x}} = \frac{1}{2\delta x} [\varphi(\mathbf{x} + \mathbf{e}_k \delta x) - \varphi(\mathbf{x} - \mathbf{e}_k \delta x)] \quad (42)$$

where the number of directional derivatives is equal to the number of moving directions \mathbf{e}_k on the lattice i.e. N_{pop} . The gradient is obtained by:

$$\nabla \varphi|_{\mathbf{x}} = 3 \sum_{k=0}^{N_{pop}} w_k \mathbf{e}_k (\mathbf{e}_k \cdot \nabla \varphi|_{\mathbf{x}}). \quad (43)$$

For the calculation of the $\nabla^2 \varphi$, all directions of propagation are taken into account by

$$(\mathbf{e}_k \cdot \nabla)^2 \varphi|_{\mathbf{x}} = \frac{1}{\delta x^2} [\varphi(\mathbf{x} + \mathbf{e}_k \delta x) - 2\varphi(\mathbf{x}) + \varphi(\mathbf{x} - \mathbf{e}_k \delta x)] \quad (44)$$

which are used to compute the laplacian:

$$\nabla^2 \varphi|_{\mathbf{x}} = 3 \sum_{k \neq 0} w_k (\mathbf{e}_k \cdot \nabla)^2 \varphi|_{\mathbf{x}}. \quad (45)$$

3.2 LBM for phase-field

For the phase-field equation, we introduce a new distribution function $g_k(\mathbf{x}, t)$ evolving with the LBE:

$$g_k(\mathbf{x} + \mathbf{c}_k \delta t, t + \delta t) = g_k(\mathbf{x}, t) - \frac{1}{\tau_g + 0.5} [g_k(\mathbf{x}, t) - g_k^{eq}(\mathbf{x}, t)] + \delta t \mathcal{G}_k(\mathbf{x}, t) \quad (46)$$

Eq. (31) is an Advection-Diffusion type Equation (ADE). The equilibrium distribution function g_k^{eq} is designed such as its moments of order zero, one, and two are respectively equal to φ , $\mathbf{u}\varphi$ and $\bar{\mathbf{I}}\varphi$ where $\bar{\mathbf{I}}$ is the identity tensor of second order:

$$g_k^{eq}(\mathbf{x}, t) = w_k \varphi \left[1 + \frac{\mathbf{c}_k \cdot \mathbf{u}}{c_s^2} \right] - \frac{\delta t}{2} \mathcal{G}_k \quad (47)$$

The first term in the right-hand side of Eq. (47) is the classical term to recover the ADE after the Chapman-Enskog procedure, and the source term \mathcal{G}_k is simply defined such as its moment of order zero is equal to $\mathcal{S}_\varphi(\varphi, \bar{\mu}^A, \bar{\mu}^B)$:

$$\mathcal{G}_k = w_k \mathcal{S}_\varphi(\varphi, \bar{\mu}^A, \bar{\mu}^B) \quad (48)$$

where \mathcal{S}_φ , defined by Eq. (35). The interface mobility $\bar{M}_\varphi = W^2/\tau_\varphi$ is a constant which is related to the relaxation rate τ_g by $\bar{M}_\varphi = \tau_g c_s^2 \delta t$. Finally, after collision and streaming, the phase-field φ is updated at each time-step by:

$$\varphi = \sum_k g_k + \frac{\delta t}{2} \mathcal{S}_\varphi \quad (49)$$

3.3 LBM for composition equations

For the treatment of the composition equations, we introduce two distribution functions $h_k^\alpha(\mathbf{x}, t)$ (for $\alpha = A, B$) which evolve with the LBE:

$$h_k^\alpha(\mathbf{x} + \mathbf{c}_k \delta t, t + \delta t) = h_k^\alpha(\mathbf{x}, t) - \frac{1}{\tau_h^\alpha(\varphi) + 0.5} [h_k^\alpha(\mathbf{x}, t) - h_k^{eq,\alpha}(\mathbf{x}, t)] \quad (50)$$

Eqs (32) look like advection-diffusion equations, but the equilibrium functions $h_k^{eq,\alpha}$ must be defined such that its moment of order two is equal to $\bar{\mathbf{I}}\bar{\mu}^\alpha$ where $\bar{\mu}^\alpha$ is related to the composition c^α (moment of order zero) by Eq. (33). In that relation, $c_0^{\alpha,eq}$ and $c_1^{\alpha,eq}$ are two scalar input values which are the two thermodynamic equilibrium compositions of each phase 0 and 1. Because the moments of order 2 differs from the moment of order 0, the equilibrium distribution function must be slightly modified compared to the classical equilibrium for an ADE by:

$$h_k^{eq,\alpha}(\mathbf{x}, t) = \begin{cases} c^\alpha - (1 - w_0)\bar{\mu}^\alpha & \text{for } k = 0 \\ w_k\bar{\mu}^\alpha + w_k c^\alpha \frac{\mathbf{c}_k \cdot \mathbf{u}}{c_s^2} & \text{for } k \neq 0 \end{cases} \quad (51)$$

In that equilibrium distribution, the moment of order zero is given by the first term of the first line and the moment of order one is given by the second term of the second line. That method is extensively used for simulating the advective Cahn-Hilliard equation ([39]). The mobility coefficients $\bar{M}^\alpha(\varphi)$ are related to the relaxation rate $\tau_h^\alpha(\varphi)$ by $\bar{M}^\alpha(\varphi) = \tau_h^\alpha(\varphi)c_s^2\delta t$. After collision and streaming, the composition is obtained by the moment of order zero of h_k^α :

$$c^\alpha = \sum_k h_k^\alpha \quad (52)$$

4 Numerical simulations

The methods of the previous section have been implemented in a C++ code: LBM.Saclay [40]. Its main feature is its multi-architecture portability by simple modifications of compilation options in the makefile. This is possible thanks to the Kokkos library [41]. Thus the same code can be run either on multi-CPU partition or on multi-GPU partition of a supercomputer. Time performances of LBM.Saclay have been compared between graphic cards and standard CPU in our previous paper [29]. Because of the efficiency of the former ones, the simulations of this work have run on the multi-GPU partitions of the supercomputers Jean-Zay (IDRIS, France) and Topaze (CCRT, France).

4.1 Ternary diffusion couple

We start by presenting a quantitative validation of the model and its implicit Gibbs-Thomson condition for a plane interface without flow. This demonstrates that the phase field model is able to reproduce the known solution of a sharp-interface problem, the symmetrical ternary diffusion couple. Phase field studies of this problem already exist in the literature, and we use this as a test for our model [42, 43]. An interface splits the infinite one-dimensional space in two domains at $x_I(t)$, with phase 0 on its left and phase 1 on its right. The interface is displaced at velocity $\dot{x}_I(t)$ by the interdiffusion of

the components. This problem can be stated as the one-dimensional free boundary problem

$$\partial_t c^\alpha = \bar{M}^\alpha \partial_{xx}^2 \bar{\mu}^\alpha, \quad x < x_I(t) \text{ or } x > x_I(t) \quad (53)$$

$$\bar{\mu}^\alpha = \bar{\mu}_{int}^\alpha, \quad x = x_I(t) \quad (54)$$

$$\dot{x}_I(c^\alpha|_{x_I^-} - c^\alpha|_{x_I^+}) = -\bar{M}^\alpha (\partial_x c^\alpha|_{x_I^-} - \partial_x c^\alpha|_{x_I^+}) \quad x = x_I(t) \quad (55)$$

$$\bar{\mu}^\alpha = \bar{\mu}_{-\infty}^\alpha \quad x = -\infty \quad (56)$$

$$\bar{\mu}^\alpha = \bar{\mu}_{+\infty}^\alpha \quad x = +\infty \quad (57)$$

with the initial conditions

$$x_I(0) = 0; \quad \bar{\mu}^\alpha = \bar{\mu}_{-\infty}^\alpha \quad (x < 0); \quad \bar{\mu}^\alpha = \bar{\mu}_{+\infty}^\alpha \quad (x > 0). \quad (58)$$

The problem corresponds to evaluating our phase field model in 1D with $\varphi = 0$ or $\varphi = 1$ and taking the interface conditions (25), (28) with $\beta = 0$ and $\kappa = 0$. In the sharp-interface view, the relation between $\bar{\mu}^\alpha$ and c^α is linear, allowing the problem to be rewritten into the classical Stefan problem in terms of either c^α or $\bar{\mu}^\alpha$ only. It is then known [44] that a self-similar solution exists with

$$x_I(t) = \xi \sqrt{t} \quad (59)$$

and

$$\bar{\mu}^\alpha(x, t) = \begin{cases} \bar{\mu}_{-\infty}^\alpha + (\bar{\mu}_{int}^\alpha - \bar{\mu}_{-\infty}^\alpha) \frac{\text{erfc}(-x/2\sqrt{M^\alpha t})}{\text{erfc}(-\xi/2\sqrt{M^\alpha})} & -\infty < x < x_I(t) \\ \bar{\mu}_{+\infty}^\alpha + (\bar{\mu}_{int}^\alpha - \bar{\mu}_{+\infty}^\alpha) \frac{\text{erfc}(x/2\sqrt{M^\alpha t})}{\text{erfc}(\xi/2\sqrt{M^\alpha})} & x_I(t) < x < +\infty \end{cases} \quad (60)$$

The statement and solution of the problem in terms of the composition fields is analogous but with a discontinuity at the interface, in coherence with chemical equilibrium. The couple of interface values $(\bar{\mu}_{int}^A, \bar{\mu}_{int}^B)$ are a solution of the system, meaning

$$\bar{\omega}_0(\bar{\mu}_{int}^A, \bar{\mu}_{int}^B) - \bar{\omega}_1(\bar{\mu}_{int}^A, \bar{\mu}_{int}^B) = 0. \quad (61)$$

A ternary system has access to a continuous set of such equilibrium couples (phase diagram tie-lines). The additional dynamical constraints select

one particular equilibrium in this continuum: the coefficient ξ is determined as the solution of a transcendental equation that couples the thermodynamic equilibrium and dynamical parameters, see Eq. (22) in [44].

To reproduce this problem numerically, the phase-field model is solved on a thin 2D domain (3000×6 LBM lattice nodes). The phase field is initialized with the equilibrium hyperbolic tangent profile. The composition fields are initialized as step functions. The parameters used are referenced in table 2 and they produce an analytical solution with $\xi = -0.269824$. Figure 2 compares the interface velocity and the concentration fields simulated with the ones expected from the analytical solution. Both are in excellent agreement, numerically confirming the interface condition (25)–(28) reconstructed by the phase field model. Note that we have chosen the system’s half-length L and the diffusion time $t_D = \min_{\alpha}(L^2/\bar{M}^{\alpha})$ as units in these comparisons.

4.2 Simulations of Ostwald ripening

Next, the phase-field model is exploited to simulate the Ostwald ripening of a set of droplets (phase 1) inside a continuous matrix (phase 0). As the Allen-Cahn model cannot describe the initial regime of phase separation from homogeneous mixtures, the initial condition starts from already developed droplets, as detailed below. In this problem, the characteristic length scale is the average spacing between droplets. However, this length is not static and increases as the growth proceeds and the droplet number decreases. In the numerical simulations, the distance between droplets is bounded by the domain size. For this reason, we once again set our numerical units of length and time as the half-length of the domain and the diffusion time, respectively, $\ell = L$ and $t_D = \min_{\alpha}(\ell^2/\bar{M}^{\alpha})$.

4.2.1 Initial condition

As already mentioned above, to study the growth kinetics, we must start from pre-existing droplets. The initial condition must be carefully constructed to satisfy the condition for growth, namely that the global composition inventory lies in the miscibility gap and that the phase fraction be sufficiently high to measure a statically relevant average. In addition, before the growth, there will be a transient regime during which the droplets reach local equilibrium with the surrounding matrix (analogous to a diffusion couple). We want the

Domain			Phase-field parameters			Transport parameters		
Symbol	Value	Dim	Symbol	Value	Dim	Symbol	Value	Dim
$[-L_x, L_x]$	$[-1, 1]$	[L]	W	1.2×10^{-3}	[L]	$(c_0^{A,\text{eq}}, c_0^{B,\text{eq}})$	(0.3, 0.3)	[-]
$[-L_y, L_y]$	$[-0.002, 0.002]$	[L]	λ	155.94541910 \cong 155.95	[-]	$(c_1^{A,\text{eq}}, c_1^{B,\text{eq}})$	(0.4, 0.4)	[-]
N_x nodes	3000	[-]	\bar{M}_φ	1.2	$[\text{L}]^2/[\text{T}]$	(\bar{M}^A, \bar{M}^B)	(1, 0.8)	$[\text{L}]^2/[\text{T}]$
N_y nodes	6	[-]				$(c^A, c^B)_{-\infty}$	(0.4, 0.175)	[-]
δx	1/1500	[L]				$(c^A, c^B)_{+\infty}$	(0.225, 0.6)	[-]
δt	1.481481×10^{-9}	[T]						

Table 2: Parameters for the simulation of symmetrical diffusion couple. λ^* is the value that cancels the kinetic coefficient β (Eq. (27)). In all simulations, that coefficient will be simply noted λ and approximated by 155.95. The values of $(c^A, c^B)_{-\infty}$ and $(c^A, c^B)_{+\infty}$ are respectively equivalent to $(\bar{\mu}^A, \bar{\mu}^B)_{-\infty} = (0.1, -0.125)$ and $(\bar{\mu}^A, \bar{\mu}^B)_{+\infty} = (-0.175, 0.2)$. The values of collision rates corresponding respectively to \bar{M}_φ , \bar{M}^A and \bar{M}^B are: $\tau_g = 0.6333$, $\tau_h^A = 0.6111$ and $\tau_h^B = 0.5888$.

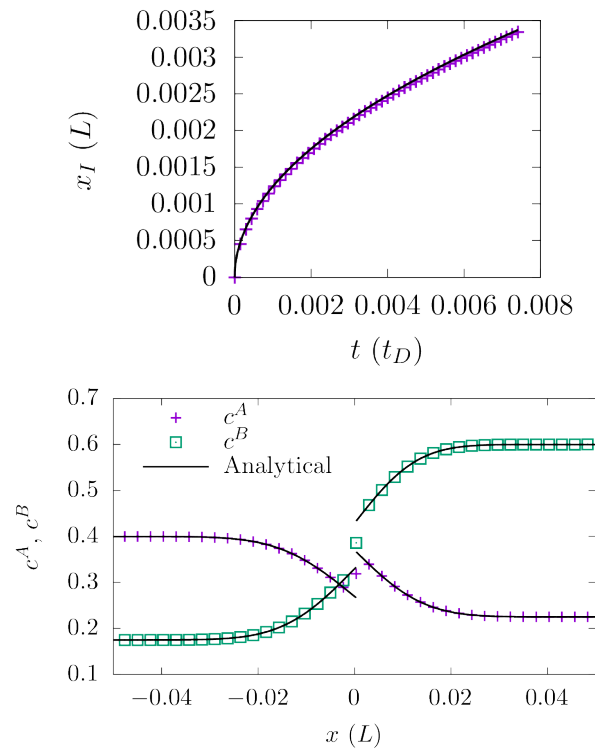


Figure 2: Benchmark of the LBM code with an analytical solution for a ternary diffusion couple. (a) Interface displacement as a function of time, (b) Composition profiles. The symbols are the simulation results, the lines the analytical predictions. All parameters are listed in Table 2.

droplets to always tend to grow during this regime, and not to shrink and risk disappearance.

We therefore choose to parametrize the initialization of the composition $\mathbf{c}(\mathbf{x}, 0)$ and the phase-field $\varphi(\mathbf{x}, 0)$ with three scalar values: the initial global composition of the system $\mathbf{c}_g = (c_g^A, c_g^B)$ and the initial phase fraction Φ of droplets. The phase-field $\varphi(\mathbf{x}, 0)$ can be easily initialized by creating spherical droplets with randomly generated positions and radii. For the compositions, we could then initialize them inside and outside those interfaces using the reference tie-line's end-points. However, specifying Φ , \mathbf{c}_g and the tie-line would overspecify the initialization because of the lever rule. Besides, if the initial composition of the matrix is at equilibrium \mathbf{c}_0^{eq} , the droplets can disappear during the transient regime. It is necessary to design an initial condition on $c^A(\mathbf{x}, 0)$ and $c^B(\mathbf{x}, 0)$ such that the droplets grow from the outset of the time evolution.

When the thermodynamic equilibrium is reached, because of the conservation rule, the global composition \mathbf{c}_g are related to the equilibrium compositions and the equilibrium phase fraction Φ^{eq} by:

$$\mathbf{c}_g = (1 - \Phi^{eq})\mathbf{c}_0^{eq} + \Phi^{eq}\mathbf{c}_1^{eq} \quad (62)$$

That relation can be inverted and yields:

$$\Phi^{eq} = \frac{|\mathbf{c}_0^{eq} - \mathbf{c}_g|}{|\mathbf{c}_0^{eq} - \mathbf{c}_1^{eq}|} \quad (63)$$

One way to avoid droplet disappearance is to initialize the system with a phase fraction of droplets Φ which is lower than the equilibrium Φ^{eq} . In that case, we need to initialize the composition in the matrix and/or in the droplets out of equilibrium (with an additional degree of freedom due to the ternary case). Here, the droplet compositions are considered at equilibrium \mathbf{c}_1^{eq} and we choose to supersaturate the matrix by offsetting its composition along the tie-line, as

$$\mathbf{c}_0^{ini} = \mathbf{c}_0^{eq} - \delta(\mathbf{c}_1^{eq} - \mathbf{c}_0^{eq}) \quad (64)$$

where the coefficient δ is defined by:

$$\delta = \frac{\Phi^{eq} - \Phi}{1 - \Phi} \quad (65)$$

where Φ^{eq} is given by Eq. (63). When $\delta > 0$ (*i.e.* when $\Phi < \Phi^{eq}$), the matrix composition is offset inside the miscibility gap. This ensures that the initial transient leading towards local equilibrium always corresponds to an increase of the global phase fraction of droplets Φ . Finally, the initial conditions of compositions write

$$\mathbf{c}(\mathbf{x}, 0) = \begin{cases} (1 - \delta)\mathbf{c}_0^{eq} + \delta\mathbf{c}_1^{eq} & \text{if } \varphi(\mathbf{x}) < 1/2 \\ \mathbf{c}_1^{eq} & \text{if } \varphi(\mathbf{x}) \geq 1/2 \end{cases} \quad (66)$$

which represents an initial supersaturation in the matrix, whereas the droplet composition is supposed to be at equilibrium.

The details of the initialization routine we used are given next. For a specified target phase fraction s , we initialize the droplet geometry according to the procedure illustrated in Figure 3 which results in lists of positions and volumes for each droplet. Then, to initialize $\varphi(\mathbf{x})$ on each lattice node, search for the closest droplet where we define the hyperbolic tangent profile using its radius and center. Next, the composition fields are initialized on each lattice node as Eq. (66) for a given composition inventory \mathbf{c}_g , followed by the chemical potential fields at equilibrium everywhere, $\bar{\mu}^\alpha(\mathbf{x}) = 0$. Finally, for simulations with flow, the flow field is initialized at rest and the pressure field at zero.

4.2.2 Geometry measurements

To measure the droplet count N , we use an algorithm for the measure of the Euler characteristic, to be understood here as the number of connected regions of $\varphi = 1$. The algorithm is adapted from reference [45] and it only requires a single pass over the lattice. The average radius $\langle R \rangle$ is measured using the integral estimate

$$\begin{aligned} \int \frac{4}{W} \varphi(1 - \varphi) d^2 \mathbf{x} &\approx \sum_i 2\pi \int_0^{+\infty} \frac{4}{W} \varphi_0(1 - \varphi_0) r dr \\ &\approx 2\pi W \sum_i \left[\frac{R_i}{W} + \mathcal{O}(e^{-4R_i/W}) \right] \\ &\approx 2\pi N \langle R \rangle \end{aligned} \quad (67)$$

where the index i stands for the droplet number. Indeed, the integrand is a function that has a sharp peak in the interfaces, and the integral approx-

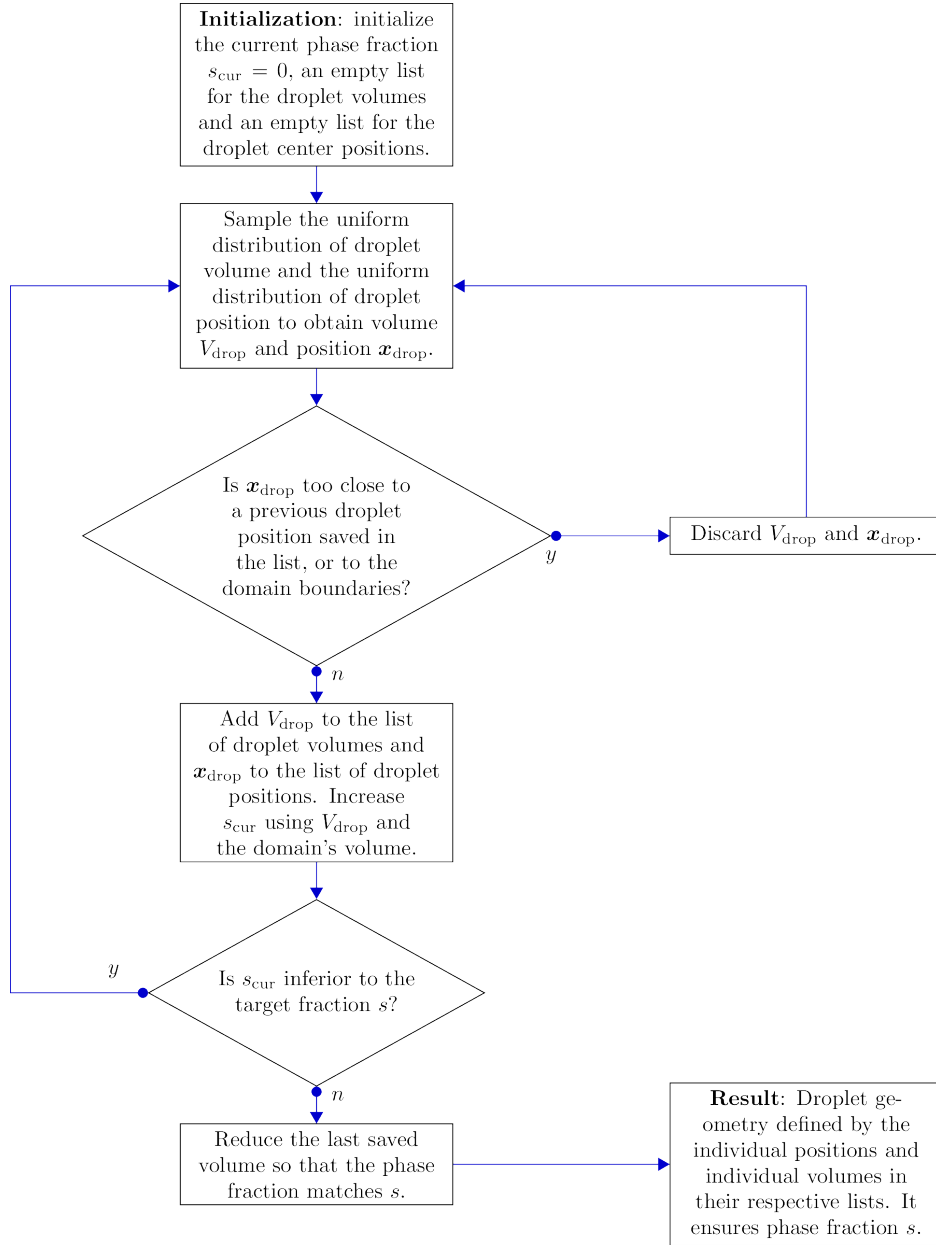


Figure 3: Procedure to initialize the droplet ensemble. Its parameters are the target phase fraction s , the domain's volume, and two uniform distributions for positions and volumes. A droplet is discarded when the sampled \mathbf{x}_{drop} is within $R_{\text{max}} + W/2$ to the domain bounds, or within twice that distance to a previous droplet's center; with R_{max} the radius corresponding to the upper bound of the volume distribution.

imately gives the total length of interface present in the system. Assuming the droplets are spherical and sufficiently far from each other, the integrals can be calculated exactly and a Taylor expansion gives the desired result, plus an error terms in $\mathcal{O}(e^{-4R_i/W})$; the numerical calculation of this integral is easy to implement and very fast (linear in lattice points and no stencil involved).

4.2.3 Ripening without flow

We first consider the ripening of a population of two-dimensional droplets without flow to test our initialization procedure and to reproduce the known growth law for $\langle R \rangle$. The domain ranges between $[-1, 1] \times [-1, 1]$ and the boundary conditions are periodic. The parameters of the simulation are listed in Table 3. The initialization produced 2737 droplets. Figure 4 shows the phase field and chemical potential fields in a small part of the domain between $[0, 0.3] \times [0, 0.45]$ containing only a small fraction of the droplet count. The phase 1 domains follow the expected evolution: the smaller droplets shrink and vanish while the larger ones grow. The chemical potentials are initialized at zero (equilibrium). The Gibbs-Thomson condition creates differences between droplets and their surrounding matrix and neighbours of different size. As the grains grow and rarify, the chemical potentials gradually homogenize. Figure 5 presents the evolution of the mean grain radius compared to a power law with exponent $1/3$. With this, we confirm the adequacy of the model to reproduce the growth kinetics.

4.2.4 Ripening and sedimentation

Next, we look at a three-dimensional ripening process including the effect of buoyancy. Table 4 lists the parameters. The gravity acts along the x -axis and the bounce-back LBM algorithm is used on the top and bottom walls, enforcing $\mathbf{u} = \mathbf{0}$ and $\nabla\varphi = \nabla c = \nabla\bar{\mu} = \mathbf{0}$. The lateral boundaries are periodic.

Figure 6 shows successive snapshot pictures of the droplet geometry. The initial condition (Figure 6a) is composed of 2035 droplets. At the beginning, diffusive Ostwald ripening takes place, and after some time (Figure 6b), the smallest droplets have vanished and the remaining ones start to sediment. The droplets then accelerate (Figure 6c), and some have already reached

Domain (D2Q9)			Phase-field parameters			Transport parameters		
Symbol	Value	Dim	Symbol	Value	Dim	Symbol	Value	Dim
$[-L_x, L_x]$	$[-1, 1]$	[L]	W	$3\delta x = 1.464 \times 10^{-3}$	[L]	$(c_0^{A,\text{eq}}, c_0^{B,\text{eq}})$	$(0.3, 0.3)$	[-]
$[-L_y, L_y]$	$[-1, 1]$	[L]	λ	155.95	[-]	$(c_{\perp}^{A,\text{eq}}, c_{\perp}^{B,\text{eq}})$	$(0.4, 0.4)$	[-]
N_x nodes	4096	[-]	\bar{M}_{φ}	1.2	$[\text{L}]^2/[\text{T}]$	$(\bar{M}_0^{AA}, \bar{M}_0^{BB})$	$(1, 0.8)$	$[\text{L}]^2/[\text{T}]$
N_y nodes	4096	[-]	Droplet initialization			$(\bar{M}_1^{AA}, \bar{M}_1^{BB})$	$(1, 0.8)$	$[\text{L}]^2/[\text{T}]$
δx	4.882×10^{-4}	[L]	(c_g^A, c_g^B)	$(0.31, 0.31)$	[-]			
δt	2.5×10^{-8}	[T]	Φ	0.08	[-]			
			$S_{\text{avg}} \pm \Delta S$	$(1.02 \pm 0.957) \times 10^{-4}$	$[\text{L}]^2$			

Table 3: Parameters for the simulation of 2D Ostwald ripening. The initial volumes of the grains are uniformly sampled in the range $[S_{\text{avg}} - \Delta S, S_{\text{avg}} + \Delta S]$. The values of collision rates corresponding respectively to \bar{M}_{φ} , \bar{M}^{AA} and \bar{M}^{BB} are: $\tau_g = 0.8776$, $\tau_h^A = 0.8146$ and $\tau_h^B = 0.7517$.

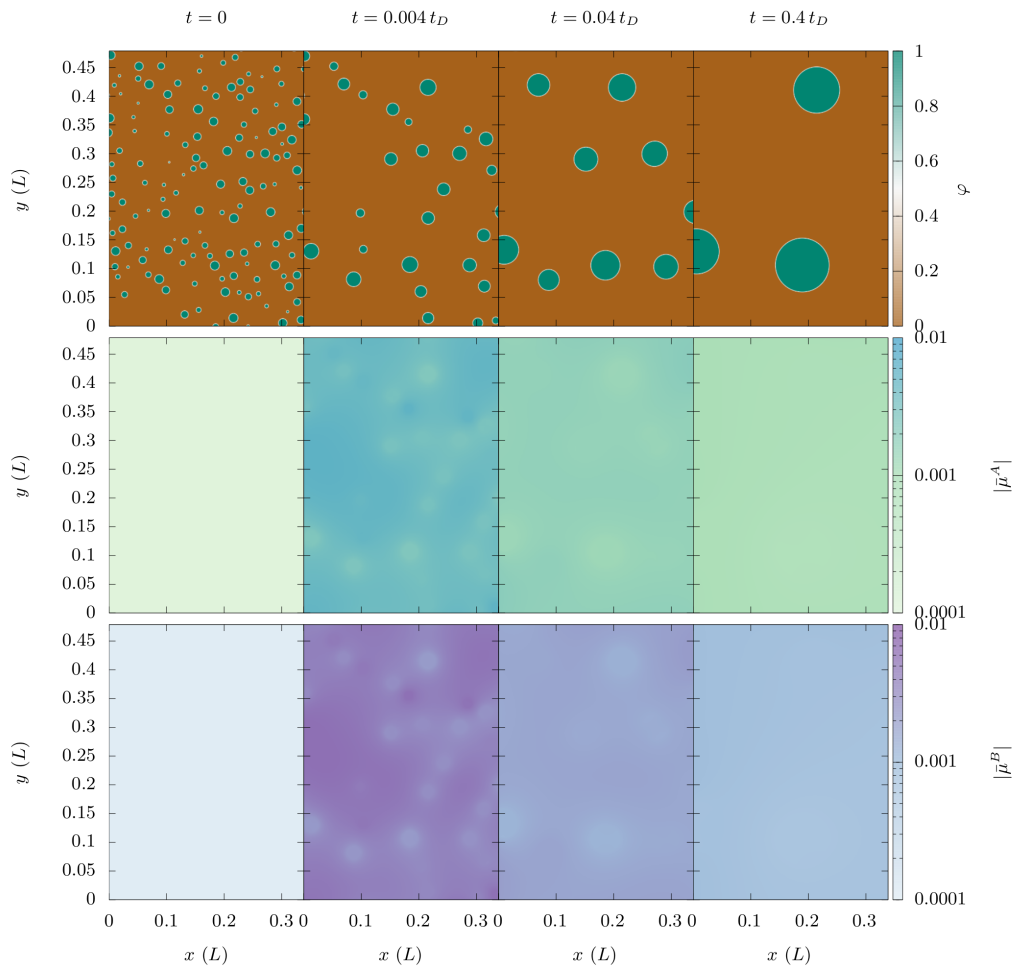


Figure 4: Heatmaps of the phase field and chemical potentials fields in a portion of the domain at various time steps during the simulation of 2D ripening without flow.

Domain (D3Q19)			Phase-field parameters			Droplet initialization		
Symbol	Value	Dim	Symbol	Value	Dim	Symbol	Value	Dim
$[-L_x, L_x]$	$[-16, 16]$	[L]	W	$4\delta x = 6.25 \times 10^{-2}$	[L]	(c_g^A, c_g^B)	$(0.32, 0.32)$	[-]
$[-L_y, L_y]$	$[-4, 4]$	[L]	λ	155.95	[-]	Φ	0.08	[-]
$[-L_z, L_z]$	$[-4, 4]$	[L]	\bar{M}_φ	1.2	$[\text{L}]^2/[\text{T}]$	$V_{avg} \pm \Delta V$	0.08 ± 0.072	$[\text{L}]^3$
N_x nodes	2048	[-]	Flow parameters			Transport parameters		
N_y nodes	512	[-]	$\rho_0 = \Delta\rho$	1	$[\text{M}]/[\text{L}]^3$	$(c_0^{A,\text{eq}}, c_0^{B,\text{eq}})$	$(0.3, 0.3)$	[-]
N_z nodes	512	[-]	ν	1	$[\text{L}]^2/[\text{T}]$	$(c_1^{A,\text{eq}}, c_1^{B,\text{eq}})$	$(0.4, 0.4)$	[-]
δx	1.5625×10^{-2}	[L]	σ	10^{-3}	$[\text{MLT}^{-2}]/[\text{L}]$	$(\bar{M}_0^{AA}, \bar{M}_0^{BB})$	$(1, 0.8)$	$[\text{L}]^2/[\text{T}]$
δt	4.2×10^{-5}	[T]	$\Delta\rho g_x$	1	$[\text{M}]/[\text{LT}]^2$	$(\bar{M}_1^{AA}, \bar{M}_1^{BB})$	$(1, 0.8)$	$[\text{L}]^2/[\text{T}]$

Table 4: Parameters for the simulation of 3D Ostwald ripening with a gravity-driven flow. The initial grains volumes are uniformly sampled in the range $[V_{avg} - \Delta V, V_{avg} + \Delta V]$. The values of collision rates corresponding respectively to ν , \bar{M}_φ , \bar{M}^{AA} and \bar{M}^{BB} are: $\tau_f = 0.6111$, $\tau_g = 0.6333$, $\tau_h^A = 0.6111$ and $\tau_h^B = 0.5888$.

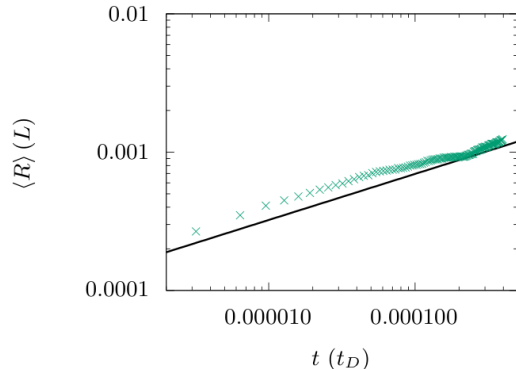


Figure 5: Mean droplet radius versus time in logarithmic scales during the Ostwald ripening simulation without flow. The green crosses are the radii measured from the simulation. The black line is a reference line for the relation $\langle R \rangle \propto t^{1/3}$.

the bottom wall. A droplet can be seen hanging from the top wall due to capillarity. Many droplets lose their spherical shape due to coalescence events. Much later (Figure 6d), the top of the domain contains almost no droplets anymore due to the combined effect of ripening, sedimentation and coalescence. A large drop of the dense phase forms. This huge mass continues to sediment, but the surrounding smaller droplets rise due to a recirculation of the flow field. At the final time of the simulation (Figure 6e), only a few droplets are left at the bottom. They are still subject to evaporation due to the very large drop that formed in the center. The flow recirculation is clearly seen at the final time step on Figure 7. At earlier times, small droplets may also be seen rising around the large domain of phase 1 before they quickly evaporate.

Figure 8(a) tracks the number of droplets in the simulation as a function of time. Around $t = 4t_D$, the very large drop forms in the center and its size becomes comparable to the system size. Hence, this single drop totally dominates the droplet distribution: the remaining droplets are few in number, and are very small in comparison (as seen in Figure 6). Because of the small system size and since all small droplets evaporate in favor of the largest drop, the growth dynamics rapidly stops to obey a power law. The development of the sedimentation dynamics is illustrated in Figure 8(b), which displays the maximum fluid velocity in the domain as a function of time. In the beginning, this maximum velocity increases monotonically: the average

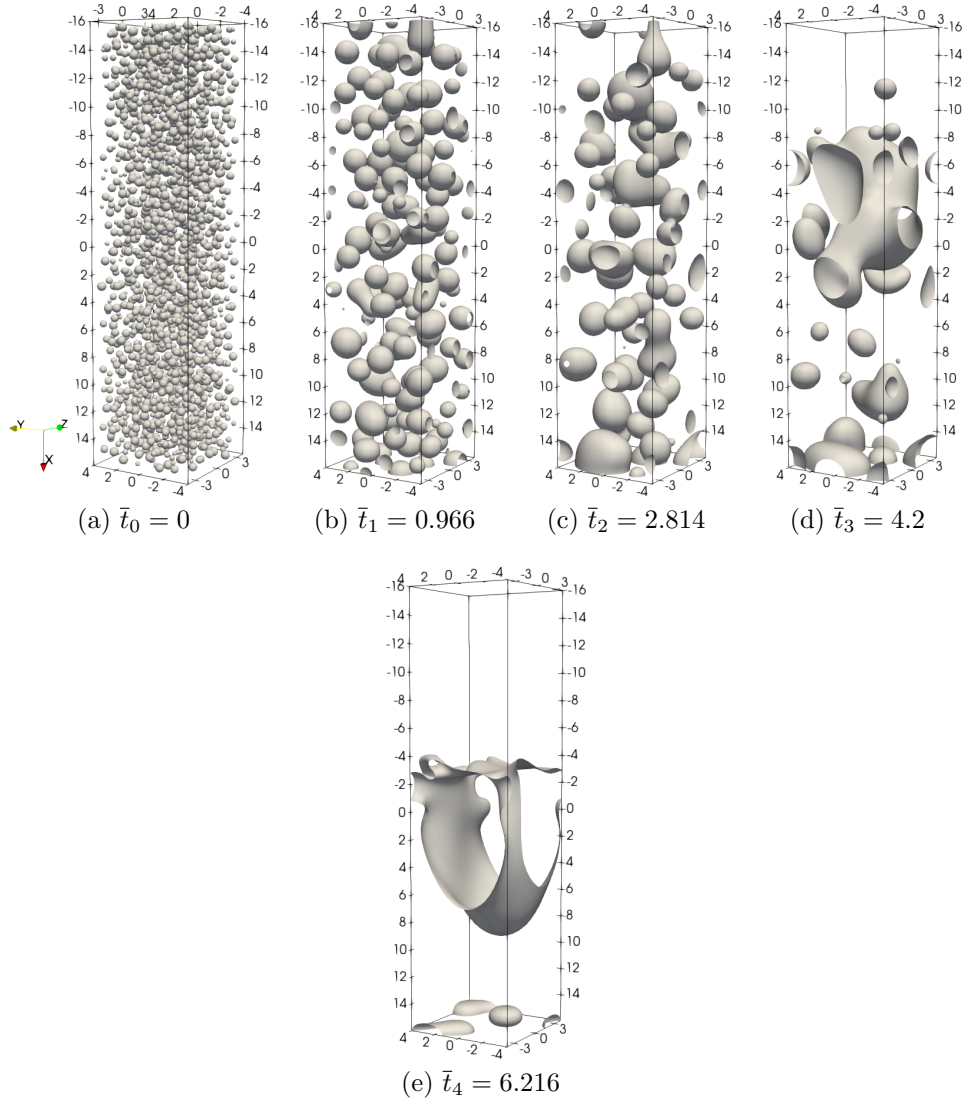


Figure 6: Three-dimensional simulation of droplet ripening with sedimentation caused by a constant gravity oriented downwards. Snapshots of the interface ($\varphi = 0.5$) at several times $\bar{t}_i = t_i/t_D$ where t_D is the diffusion time $t_D = \ell^2/\bar{M}^A$ with $\ell = 4$ and $\bar{M}^A = 1$. The simulation outputs t_i are ($\times 10^5 \delta t$): $t_1 = 3.68$, $t_2 = 10.72$, $t_3 = 16$ and $t_4 = 23.68$. The simulation took 24h on 64 GPU A100.

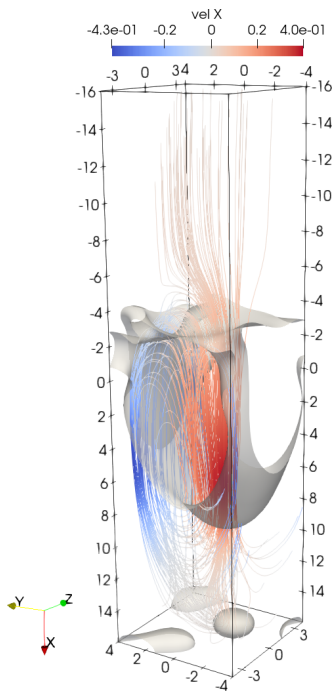


Figure 7: Streamlines at the final time of droplet ripening with sedimentation. The streamlines are colored by the velocity component along the x -axis, showing the recirculation around the large falling drop.

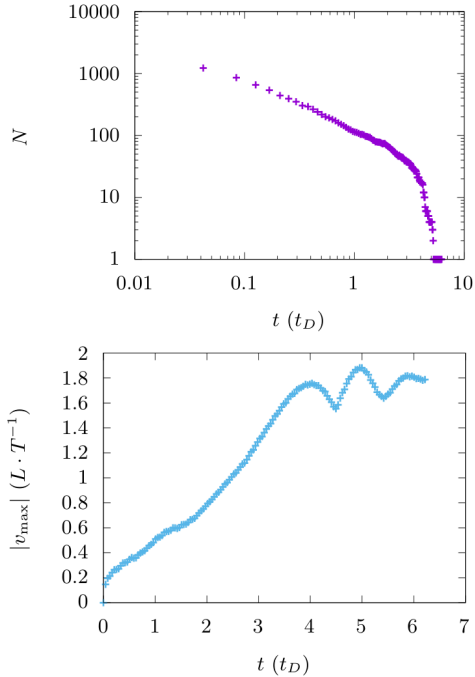


Figure 8: Droplet count (a) and maximum fluid velocity (b) as a function of time during the simulation of Figure 6.

droplet size increases with time, which leads to higher sedimentation velocities. After the formation of the large drop at $t = 4t_D$, the velocity saturates and oscillates. In this regime, the finite system size limits the sedimentation velocity of the central drop, and the highest velocities occur in the upward recirculation.

5 Conclusion and outlook

We have constructed and tested a model for the simulation of late-stage coarsening in phase-separating liquids, taking into account buoyancy effects which lead to droplet sedimentation. Two-phase coexistence and the motion of interfaces are described by a grand-canonical phase-field model, which can be adapted to arbitrary thermodynamic properties as described by a free-energy model. The coupled model is simulated numerically by the lattice-Boltzmann method, which is used to integrate in time all equations of the model. This

makes the simulation code monolithic despite its multiphysics nature. Therefore, it is particularly well adapted for high-performance simulations on GPU architectures.

We have demonstrated the capabilities of our approach by several test cases. In Section 4 we started by verifying that this model reconstructs the correct coupling between interface kinetics and thermodynamics of a three-components system when compared with the equivalent sharp-interface problem. Next, simulations of Ostwald ripening have been carried out in two dimensions in a large system, and we have verified that the mean droplet radius follows the expected power law with time. Finally, one large-scale three-dimensional simulation of simultaneous coarsening and droplet sedimentation has been performed. It has demonstrated that our model can be used to study the interplay between coarsening and fluid flow created by droplet sedimentation.

With respect to a multi-component Cahn-Hilliard model, our approach has at least two advantages: as already stated, it can be adapted to simulate any desired substance for which free-energy data are available, without restrictions on the choice of the surface tension. Furthermore, the equations of the phase-field model are second order in space, rather than the fourth order Cahn-Hilliard equation, which makes its numerical integration more efficient. The price to pay is that the initial stages of phase separation cannot be described by this model, which makes it necessary to construct an initial state *ad hoc* by making hypotheses on the initial droplet size distribution. However, since the memory of the initial state is rapidly lost during the coarsening of a disordered droplet distribution, this should not be a severe problem.

We have written down a model for a ternary mixture here, but there is no difficulty in generalizing the approach to mixtures with more than three components, as long as the necessary thermodynamic and kinetic data (free energies and mobilities) are available. An interesting question that could be studied in the future is the interplay between coarsening and sedimentation in the macroscopic redistribution of components: since the sedimentation of the droplets leads to an accumulation of the denser phase at the bottom of the system, and the sedimentation velocity is linked to the droplet size, there is a non-trivial coupling between the two phenomena.

Acknowledgements

This work was granted access to the HPC resources of IDRIS (super-computer Jean-Zay, partition V100) and CCRT (Topaze, partition A100). Alain Cartalade wishes to thank the SIVIT project involving Orano and EDF for the financial support.

References

- [1] JD Gunton, M San Miguel, and PS Sahni. The dynamics of first-order phase transitions. In C. Domb and J. L. Lebowitz, editors, *Phase Transitions and Critical Phenomena, Vol. 8*, pages 267–466, New York, 1983. Academic Press.
- [2] Eric D. Siggia. Late stages of spinodal decomposition in binary mixtures. *Phys. Rev. A*, 20:595–605, Aug 1979.
- [3] A.J. Bray. Theory of phase-ordering kinetics. *Advances in Physics*, 43(3):357–459, 1994.
- [4] A. J. Bray. Theory of phase-ordering kinetics. *Advances in Physics*, 51(2):481–587, 2002.
- [5] Stephane Gin, Patrick Jollivet, Magaly Tribet, Sylvain Peugot, and Sophie Schuller. Radionuclides containment in nuclear glasses: an overview. *Radiochimica Acta*, 105(11):927–959, 2017.
- [6] Sophie Schuller, Olivier Pinet, and Bruno Penelon. Liquid–liquid phase separation process in borosilicate liquids enriched in molybdenum and phosphorus oxides. *Journal of the American Ceramic Society*, 94(2):447–454, 2011.
- [7] O. Pinet, J.-F. Hollebecque, I. Hugon, V. Debono, L. Campayo, C. Vallat, and V. Lemaitre. Glass ceramic for the vitrification of high level waste with a high molybdenum content. *Journal of Nuclear Materials*, 519:121–127, 2019.
- [8] J. W. Cahn and J. E. Hilliard. Free energy of a non-uniform system. 1. interfacial free energy. *J. Chem. Phys.*, 28:258–267, 1958.

- [9] J.U Brackbill, D.B Kothe, and C Zemach. A continuum method for modeling surface tension. *Journal of Computational Physics*, 100(2):335–354, 1992.
- [10] David Jacqmin. Calculation of two-phase navier–stokes flows using phase-field modeling. *Journal of Computational Physics*, 155(1):96–127, 1999.
- [11] Hervé Henry and György Tegze. Self-similarity and coarsening rate of a convecting bicontinuous phase separating mixture: Effect of the viscosity contrast. *Phys. Rev. Fluids*, 3:074306, Jul 2018.
- [12] Hervé Henry and György Tegze. Kinetics of coarsening have dramatic effects on the microstructure: Self-similarity breakdown induced by viscosity contrast. *Phys. Rev. E*, 100:013116, Jul 2019.
- [13] Ciro Semprebon, Timm Krüger, and Halim Kusumaatmaja. Ternary free-energy lattice boltzmann model with tunable surface tensions and contact angles. *Phys. Rev. E*, 93:033305, Mar 2016.
- [14] M.A. Rasolofomanana, C. Cardon, M. Plapp, T. Philippe, H. Henry, and R. Le Tellier. Diffuse-interface modelling of multicomponent diffusion and phase separation in the u-o-zr ternary system. *Computational Materials Science*, 214:111650, 2022.
- [15] N. Provatas and K. Elder. *Phase-field methods in materials science and engineering*. Wiley-VCH, Weinheim, 2010.
- [16] I. Steinbach. Phase-field models in materials science. *Model. Simul. Mater. Sci. Eng.*, 17(7):073001, 2009.
- [17] M. Plapp. Phase-field models. In T. Nishinaga, editor, *The Handbook of Crystal Growth, 2nd edition, Vol. 1B*, pages 631–668, Amsterdam, 2015. Elsevier.
- [18] Alain Karma and Wouter-Jan Rappel. Quantitative phase-field modeling of dendritic growth in two and three dimensions. *Phys. Rev. E*, 57:4323–4349, Apr 1998.
- [19] Robert F. Almgren. Second-order phase field asymptotics for unequal conductivities. *SIAM Journal on Applied Mathematics*, 59(6):2086–2107, 1999.

- [20] Blas Echebarria, Roger Folch, Alain Karma, and Mathis Plapp. Quantitative phase-field model of alloy solidification. *Phys. Rev. E*, 70:061604, Dec 2004.
- [21] Arnaldo Badillo. Quantitative phase-field modeling for boiling phenomena. *Phys. Rev. E*, 86:041603, Oct 2012.
- [22] Seong Gyoon Kim, Won Tae Kim, and Toshio Suzuki. Phase-field model for binary alloys. *Phys. Rev. E*, 60:7186–7197, Dec 1999.
- [23] Mathis Plapp. Unified derivation of phase-field models for alloy solidification from a grand-potential functional. *Phys. Rev. E*, 84:031601, Sep 2011.
- [24] A. Choudhury and B. Nestler. Grand-potential formulation for multi-component phase transformations combined with thin-interface asymptotics of the double-obstacle potential. *Phys. Rev. E*, 85:021602, 2012.
- [25] M. Plapp. Phase-field modelling of solidification microstructures. *Journal of the Indian Institute of Science*, 96(3):179–198, 2016.
- [26] Timm Krüger, Halim Kusumaatmaja, Alexandr Kuzmin, Orest Shardt, Goncalo Silva, and Erlend Magnus Viggen. *The Lattice Boltzmann Method: Principles and Practice*. Springer International Publishing, Cham, 2017.
- [27] Larry Kaufman and Henry L. Bernstein. *Computer calculation of phase diagrams with special reference to refractory metals*. New York : Academic Press, 1970.
- [28] Alain Cartalade, Amina Younsi, and Mathis Plapp. Lattice boltzmann simulations of 3d crystal growth: Numerical schemes for a phase-field model with anti-trapping current. *Computers & Mathematics with Applications*, 71(9):1784–1798, 2016.
- [29] Werner Verdier, Pierre Kestener, and Alain Cartalade. Performance portability of lattice boltzmann methods for two-phase flows with phase change. *Computer Methods in Applied Mechanics and Engineering*, 370:113266, 2020.

- [30] J. S. Langer. An introduction to the kinetics of first-order phase transitions. In C. Godrèche, editor, *Solids far from equilibrium*, Edition Aléa Saclay, pages 297–363, Cambridge, UK, 1991. Cambridge University Press.
- [31] R. Bayle, O. Cueto, S. Blonkowski, T. Philippe, H. Henry, and M. Plapp. Phase-field modeling of the non-congruent crystallization of a ternary Ge–Sb–Te alloy for phase-change memory applications. *Journal of Applied Physics*, 128(18):185101, November 2020.
- [32] Raphael Bayle. *Simulation des mécanismes de changement de phase dans des mémoires PCM avec la méthode multi-champ de phase*. PhD thesis, 2020. Thèse de doctorat dirigée par Plapp, Mathis, Institut polytechnique de Paris 2020.
- [33] R. Folch, J. Casademunt, A. Hernández-Machado, and L. Ramírez-Piscina. Phase-field model for hele-shaw flows with arbitrary viscosity contrast. ii. numerical study. *Phys. Rev. E*, 60:1734–1740, Aug 1999.
- [34] Y. Sun and C. Beckermann. Sharp interface tracking using the phase-field equation. *Journal of Computational Physics*, 220(2):626–653, jan 2007.
- [35] Xiaoyi He, Xiaowen Shan, and Gary D. Doolen. Discrete boltzmann equation model for nonideal gases. *Phys. Rev. E*, 57:R13–R16, Jan 1998.
- [36] X. He and L.-S. Luo. Lattice boltzmann model for the incompressible navier-stokes equation. *Journal of Statistical Physics*, 88(3/4):pp. 927–944, 1997.
- [37] Y. Q. Zu and S. He. Phase-field-based lattice boltzmann model for incompressible binary fluid systems with density and viscosity contrasts. *Phys. Rev. E*, 87:043301, Apr 2013.
- [38] Abbas Fakhari, Travis Mitchell, Christopher Leonardi, and Diogo Bolster. Improved locality of the phase-field lattice-boltzmann model for immiscible fluids at high density ratios. *Phys. Rev. E*, 96:053301, Nov 2017.

- [39] Abbas Fakhari and Mohammad H. Rahimian. Phase-field modeling by the method of lattice boltzmann equations. *Phys. Rev. E*, 81:036707, Mar 2010.
- [40] LBM_Saclay code. https://gitlab.maisondelasimulation.fr/users/sign_in, 2018.
- [41] H. Carter Edwards, Christian R. Trott, and Daniel Sunderland. Kokkos: Enabling manycore performance portability through polymorphic memory access patterns. *Journal of Parallel and Distributed Computing*, 74(12):3202 – 3216, 2014. Domain-Specific Languages and High-Level Frameworks for High-Performance Computing.
- [42] J. Heulens, B. Blanpain, and N. Moelans. Phase-field analysis of a ternary two-phase diffusion couple with multiple analytical solutions. *Acta Materialia*, 59(10):3946 – 3954, 2011.
- [43] Arka Lahiri, T. A. Abinandanan, and Abhik Choudhury. Theoretical and numerical study of growth in multi-component alloys. *Metallurgical and Materials Transactions A*, 48:4463–4476, October 2017.
- [44] P. Maugis, W.D. Hopfe, J.E. Morral, and J.S. Kirkaldy. Multiple interface velocity solutions for ternary biphasic infinite diffusion couples. *Acta Materialia*, 45(5):1941 – 1954, 1997.
- [45] Rafael Wiemker. Total Euler Characteristic as a Noise Measure to aid Transfer Function Design. In Mario Hlawitschka and Tino Weinkauff, editors, *EuroVis - Short Papers*. The Eurographics Association, 2013.